CHEMISTRY OF MATERIALS
Cite This: Chem. Mater. 2020, 32, 400−409
Article
pubs.acs.org/cm

Understanding the Enhanced Stability of Bromide Substitution in Lead Iodide Perovskites

Alex Aziz,[†,§] Nicholas Aristidou,[‡,§] Xiangnan Bu,[‡] Robert J. E. Westbrook,[‡] Saif A. Haque,*[,‡] and M. Saiful Islam*[,†]

[†]Department of Chemistry, University of Bath, Bath BA2 7AY, U.K.
[‡]Department of Chemistry, Imperial College London, London SW7 2AZ, U.K.

Supporting Information

ABSTRACT: Lead halide perovskites have rapidly emerged as candidate materials for high-performing solar cells, but show serious issues related to long-term stability. Methylammonium (MA) lead perovskites with mixed iodide−bromide compositions, $MAPb(I_{1-x}Br_x)_3$, are reported to exhibit improved stability, but the origin of such behavior is not fully understood. Here, we report new insights into the degradation properties of $MAPb(I_{1-x}Br_x)_3$ using ab initio simulations and a range of spectroscopic techniques. Absorbance spectroscopy shows that as the Br content increases, the material stability toward oxygen and light increases. Isothermal gravimetric analysis and time-resolved single photon counting show that the amount of oxygen incorporation into perovskite films decreases significantly with increasing Br content. Ab initio simulations indicate that the degradation reaction involving superoxide species is energetically exothermic for pure $MAPbI_3$ but becomes less favorable with increasing Br content with an endothermic energy for pure $MAPbBr_3$, suggesting that the degradation of $MAPbBr_3$ in the presence of oxygen and light is unfavorable. The simulations indicate shorter N−H...Br hydrogen bonds between the MA^+ cation and Br ions, which would promote greater structural stability upon bromide substitution. Thin-film passivation with iodide salts is shown to enhance the stabilities of mixed-halide perovskite films and solar cell devices. The greater fundamental understanding of mixed iodide−bromide systems gained from this study is important for the future design of stable perovskite solar cells.

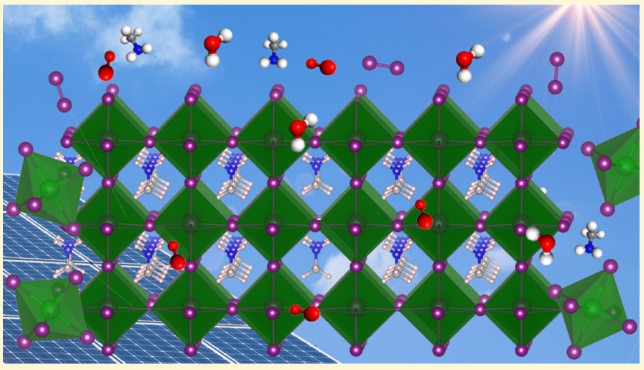

INTRODUCTION

Hybrid lead halide perovskites have been generating enormous interest over the past few years for use in low-cost and solution-processable solar cells, as well as the recent avenue of perovskite−silicon tandem cells.[1−18] Of particular interest has been methylammonium lead iodide ($MAPbI_3$), which has demonstrated promising results in terms of photovoltaic performance in a wide range of device architectures.[1−4] However, an important issue regarding its commercial application is its long-term material stability under ambient operating conditions.

There are a number of factors that affect the degradation of perovskite solar cells, namely, moisture, temperature, and UV illumination.[19−31] In previous studies,[32−34] we have demonstrated that when $MAPbI_3$ is exposed to oxygen and light, a photodegradation process occurs via the formation of superoxide species. From these initial findings, a technique to passivate vacancy defects was reported, involving post-treatment with an iodide salt resulting in enhanced film and device stability.[32]

Recent studies have observed that anion substitution (bromide for iodide) to create mixed-halide perovskite films generates longer operational lifetimes and high power conversion efficiencies.[35−42] In particular, $MAPb(I_{1-x}Br_x)_3$ has been reported to show enhanced stability toward ambient conditions and increased moisture tolerance when the bromide content is increased,[35,43−50] although for intermediate compositions ($x = 0.5$), there are reports of halide segregation. This is detected by X-ray diffraction (XRD), indicating that any changes to the crystal structure that occur due to the irradiation of the crystal structure can have an impact on the overall results.[51−57]

Herein, we investigate the mixed-halide system $MAPb(I_{1-x}Br_x)_3$ with the overall aim of understanding the key factors behind the enhanced stability in such materials, using a range of computational and experimental techniques, such as UV/vis, fluorescence, time-resolved photoluminescence (TRPL), transient absorption spectroscopy (TAS), and density functional theory (DFT) simulations. These techniques were selected as they have previously been shown to help identify the rate of degradation and the yield of superoxide along with the impact on charge separation going beyond our previous work.[32−34,58] We show that as the bromide content is increased, the yield of

Received: September 29, 2019
Revised: December 8, 2019
Published: December 9, 2019

DOI: 10.1021/acs.chemmater.9b04000
Chem. Mater. 2020, 32, 400−409

superoxide species decreases and consequently the material stability toward oxygen and light also increases. In addition, we investigate the energetics of degradation reactions and the role that iodide salt treatment can play in obtaining more stable mixed-halide perovskite films and solar cell devices.

RESULTS AND DISCUSSION

Bromide Substitution and Superoxide Yields. We first assess the stability of $MAPb(I_{1-x}Br_x)_3$ perovskite films deposited on glass substrates toward dry air (oxygen) and light, by employing UV/vis spectroscopy to monitor the degradation. The method used is in accordance with our previous work, where a selected wavelength is used to monitor the transformation from the starting material to the degradation products.[32,33] This is possible as the degradation mechanism results in a color change from the dark perovskite phase to a yellow lead iodide phase. Samples with a range of values from x = 0.0 to 1.0 were selected to explore the impact of bromide substitution on stability toward the degradation conditions. The absorption spectra of the mixed-halide perovskite samples studied are shown in Figure 1a.

We now consider the effect of light and oxygen on the stability of $MAPb(I_{1-x}Br_x)_3$ perovskite films. The UV−vis absorption spectroscopy measurements presented in Figure 1b highlight that in all cases where iodide is present, degradation occurs. Importantly, the time taken for the perovskite sample to degrade increases with increasing bromide content. To emphasize this, the pristine $MAPbI_3$ film ($x = 0$) completely degrades within 100 h, while at x = 0.75, degradation takes over 400 h. Furthermore, when no iodide is present, minimal observable degradation is seen over the experimental time frame. These observations suggest that film stability can be enhanced by bromide substitution, and this has important implications for the enhanced stability of solar cell devices.

The mechanisms behind the enhanced stability of $MAPbBr_3$ to light and oxygen may be attributed to a number of factors: the generation of superoxide species, the thermodynamics of the degradation process, and the differences in oxygen incorporation into the film. First, to probe the effect of superoxide generation as a function of bromide content, we measure the yield of photoinduced superoxide. Figure 1c shows the superoxide yields measured for the same film compositions explored in Figure 1a. The data collected shows that increasing bromide content reduces superoxide yields.

Next, we seek to understand how the role of oxygen diffusion into films may be impacted by bromide substitution and if this can also account for the enhanced stability reported in Figure 1. To investigate this, we used a combination of isothermal gravimetric analysis (IGA)[32] and photoluminescence spectroscopy. In the IGA experiment, samples were prepared and sealed in an inert atmosphere, and then the weight increase was measured as a function of time under oxygen flux into the chamber. The data presented in Figure 2a and Table S1 of the Supporting Information shows an inverse correlation between the bromide content and oxygen incorporation into the film. It appears that exchanging iodide for bromide leads to less oxygen stored within films, which can, in part, account for the reduced superoxide yields observed for higher substitution levels.

To further probe this effect, we used photoluminescence (PL) spectroscopy, which gives us a depth-selective probe of O_2 ingress. By exciting the perovskite at a wavelength of 404 nm, at which the penetration depth of light is estimated to be 10 nm, we are able to obtain specific PL information from the desired face

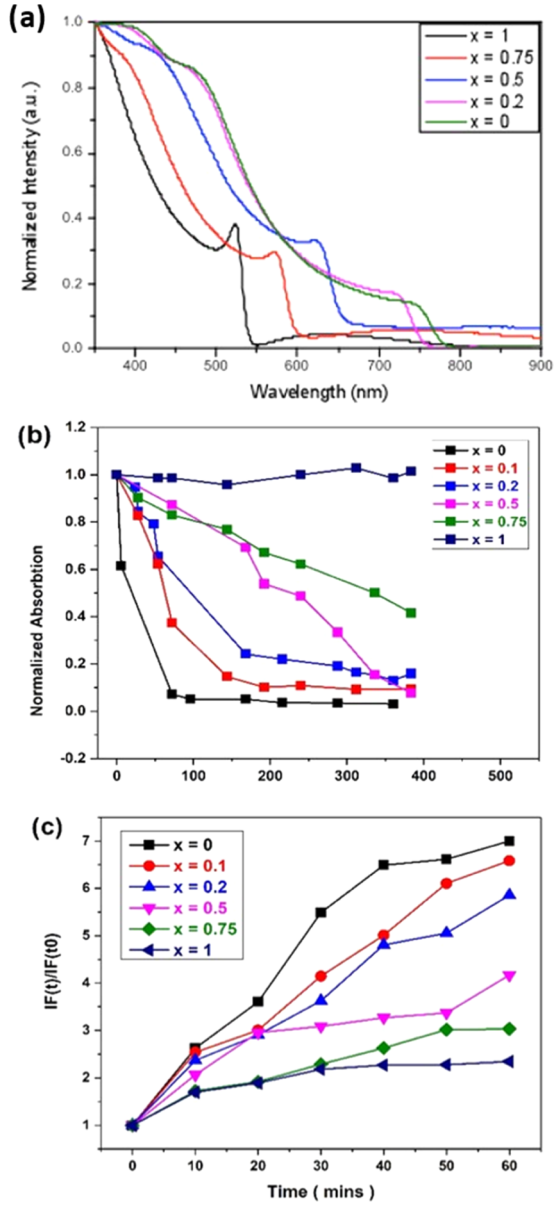

Figure 1. (a) Raw absorbance spectra for pristine films before degradation; (b) normalized absorbance decays as a function of aging under oxygen and light conditions for $MAPb(I_{1-x}Br_x)_3$, where x = 0, 0.1, 0.2, 0.5, 0.75, and 1. Films become more stable as the bromine content increases; (c) superoxide yield generation (raw data, as collected) for the same film compositions. Superoxide yields decrease as the bromide content increases. Note that the data shown in (c) is presented in the form: superoxide yield (normalized for photons absorbed) versus time as in our previous work by Pont et al.[35]

of the perovskite film.[59] Moreover, the interaction between O_2 and $MAPbX_3$ is known to increase the PL signal on account of a passivation effect.[60,61] Therefore, by probing the PL signal from the substrate of the sample (furthest from the air interface) as a function of time in O_2, we can ascertain how easily O_2 propagates through the films. In light of this, Figure 2b shows that oxygen is incorporated into $MAPbI_3$ films, as evidenced by the rapid increase in PL. It is also evident that when a higher content of Br is present in the films, this effect is subdued. In fact, no increase in PL is observed in the case of $MAPbBr_3$. It is important to note that when the $MAPbBr_3$ was probed at the surface (Figure S1), there was a significant increase in PL. This

DOI: 10.1021/acs.chemmater.9b04000
Chem. Mater. 2020, 32, 400−409

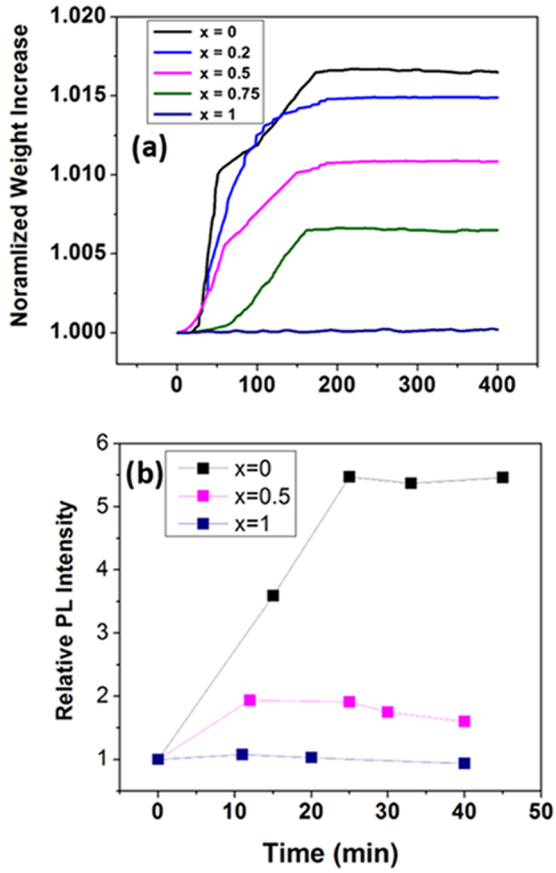

Figure 2. Oxygen ingress in $CH_3NH_3Pb(I_{1-x}Br_x)_3$ films. (a) Isothermal gravimetric analysis (IGA) traces of $CH_3NH_3Pb(I_{1-x}Br_x)_3$ films after exposure to dry air flux. (b) Normalized photoluminescence intensity obtained from samples pumped with a 404 nm laser incident on the substrate face of the perovskite. The increase of this intensity is shown over time after exposure to ambient air in the dark.

data implies that oxygen is present at the surface of the $MAPbBr_3$ film but is blocked from entering the interior of the sample.

Degradation Reaction Energetics and Structural Effects. To complement the experimental work, ab initio simulation techniques were used to investigate the effects of bromide substitution on the degradation process, building on our previous successful computational studies.[32,62−64] We first explored the degradation pathway leading to water and lead halide formation in the presence of oxygen

$$4CH_3NH_3PbX_3 + O_2 \rightarrow 4PbX_2 + 2X_2 + 2H_2O + 4CH_3NH_2 \quad (1)$$

where an O_2 molecule is introduced onto the same I vacancy site in all compositions apart from the pure Br composition, in which the site is a Br vacancy.

Figure 3 shows the reaction energies as a function of the Br content in $MAPb(I_{1-x}Br_x)_3$ with full data given in Table S2. For $MAPbI_3$, the energy of reaction 1 is calculated to be 1.56 eV per oxygen molecule, indicating that the degradation process in the absence of light is unfavorable, which is consistent with observation and previous work.[32] In addition, the energy for this degradation reaction 1 for $MAPbBr_3$ is even more unfavorable, with a calculated value of 4.98 eV, which points to the enhanced stability of this perovskite. In our analysis, we use the configuration with the highest probability of occurrence

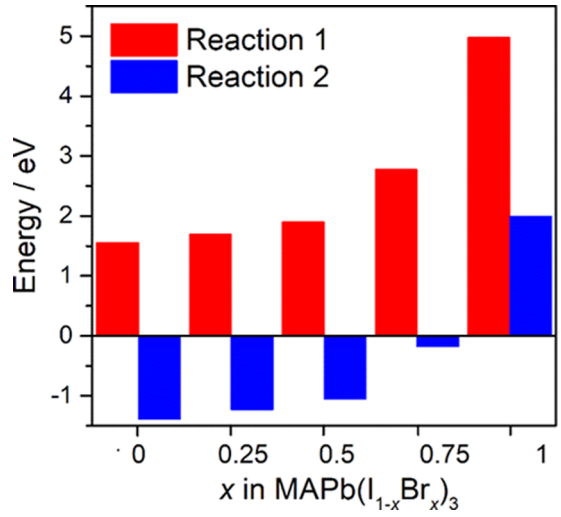

Figure 3. Calculated energies for the degradation reactions (eqs 1 and 2) as a function of the Br content for $MAPb(I_{1-x}Br_x)_3$.

at 300 K in the mixed systems, with the number of equivalent and inequivalent configurations given in Table S3. We have calculated the average lattice parameters as a function of composition (Figure S2), as well as the energy of mixing (Figure S3). Our results suggest the complete mixing of Br and I, which are stabilized by entropic effects. We note that there has been a debate concerning mixed-halide phase segregation, especially in the $MAPb(I_{0.5}Br_{0.5})_3$ composition.[51]

As suggested in recent work,[30] we also investigated the degradation pathway where O_2 acts as a catalyst, degrading methylammonium ions into methylamine and hydrogen. We find this reaction to be ∼5 eV higher in energy than degradation through water formation, indicating that the process is much less favorable.

For degradation to occur, the film must be exposed to O_2 and light. Under illumination, O_2 acts as an electron scavenger absorbing photoexcited electrons to form superoxide species. The next step would be for superoxide to react with the positively charged photo-oxidized perovskite, indicated by * in the following equation

$$4CH_3NH_3PbX_3^* + O_2^- \rightarrow 4PbX_2 + 2X_2 + 2H_2O + 4CH_3NH_2 \quad (2)$$

Degradation of $MAPbI_3$ is now found to be favorable, with a reaction energy of −1.39 eV per superoxide ion. In contrast, for $MAPbBr_3$, the degradation reaction is found to be unfavorable with an endothermic reaction energy of 2.00 eV (Figure 3). This is consistent with our experimental results that show O_2/light degradation of $MAPbI_3$ and enhanced stability of $MAPbBr_3$ (Figure 1c). For comparison, we also show the calculated reaction energies for the mixed-anion phases $MAPb(I_{1-x}Br_x)_3$, indicating that the degradation reaction in the presence of superoxide becomes less favorable with increasing Br content. This directly supports our experimental results of enhanced film stability with increasing bromide content. In the mixed systems, we find that the lowest energy degradation pathway leads to the formation of $PbBr_2$ and I_2. We note that the previous calculations[40] on the phase diagram for $MAPb(I_{1-x}Br_x)_3$ reveal a thermodynamic metastability for intermediate I/Br compositions.

DOI: 10.1021/acs.chemmater.9b04000
Chem. Mater. 2020, 32, 400−409

Other factors that could also contribute to the stability of $MAPbBr_3$ are changes in the hydrogen bonding between the methylammonium cation and the anion lattice, or a decrease in the optical absorbance of the perovskite. Comparing the end members $MAPbI_3$ and $MAPbBr_3$, in which there is complete substitution of iodide with the smaller bromide ion, the calculated cell volume is reduced by 15.8%, which is in agreement with the experimentally reported values of up to 17% (Figure S2).[65,66] XRD diffraction gives Pb−I and Pb−Br bond lengths of 3.16 and 2.97 Å, respectively.[67,68] These values are in line with our calculated bond lengths of 3.21 and 3.00 Å, suggesting stronger Pb−Br bonds that need to be broken in the degradation process. Our DFT simulations indicate that this contraction also leads to shorter H-bond distances between the NH_3 groups and Br ions, as shown in Figure 4. Consistent with

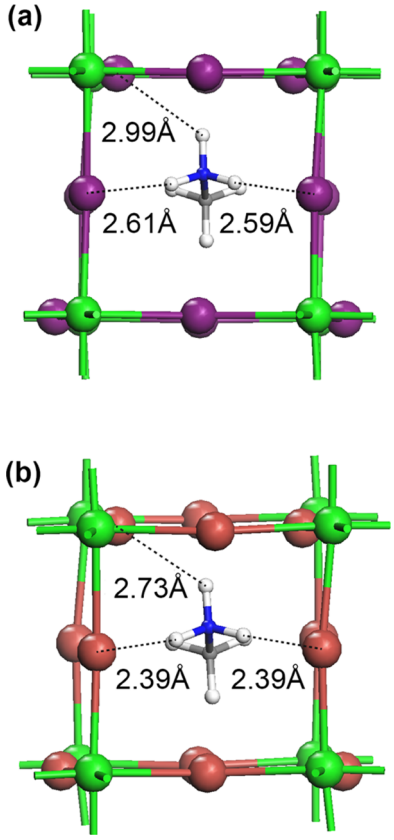

Figure 4. Calculated local structures highlighting the hydrogen bonding between HN and X in (a) tetragonal $MAPbI_3$ and (b) tetragonal $MAPbBr_3$. The H_C−X distances are calculated to be greater than 3 Å and so do not form. Key: Pb (green), I (purple), Br (orange), N (blue), C (gray), H (white).

our simulation results, XRD and Raman studies[41] find the shortest H−Br bond distance of 2.36 Å in the tetragonal phase (between about 140 and 230 K) and 2.46 Å in the cubic phase, above 230 K (Table S4). Such structural effects would result in stronger H-bonding in $MAPbBr_3$ and hence impart greater structural stability. We also find that the H−X distance between the CH_3 group and the Br is greater than 3 Å, showing that they do not form H-bonds, which is in agreement with Yin et al. who report that CH_3−Br hydrogen bonds only form in the orthorhombic phase of $MAPbBr_3$.[41]

The contraction of the perovskite lattice also suggests an additional factor in the enhanced stability of Br-containing samples through the restriction of O_2 diffusion through the film. This is further supported by scanning electron microscope images reported by Atourki et al. who show that in contrast to $MAPbI_3$ thin films, which form fiber-like crystals with voids between them, $MAPbBr_3$ form larger aggregate crystals, which would further limit diffusion.[65] Indeed, the combination of the findings in this section and Figure 2 suggests that O_2 is less able to penetrate the interior of Br-rich films on account of the smaller unit cell providing a physical barrier to O_2 diffusion. Interestingly, such a structural contraction in $MAPbBr_3$ would also inhibit MA^+ migration in comparison to that in $MAPbI_3$, which warrants further investigation.

Film Passivation via Salt Treatments. The enhanced stability of mixed-halide perovskites makes them more desirable for solar cell applications. However, as the bromide content increases, the optical properties become less favorable for efficient photovoltaic devices. For example, the absorbance data (Figure 1a) shows that upon increasing the bromide content, the band edge shifts and there is less absorption at higher wavelengths, which translates to less efficient solar cell devices. Consequently, we now consider if we can further enhance the stability of the mixed-halide perovskites by surface passivation via iodide salt treatments.[35] Of particular interest are the lower bromide content films as they allow the stability to be optimized while maximizing the spectral characteristics for light harvesting. In these experiments, we employed methylammonium iodide (MAI) as a coating agent with concentrations of 0.01, 0.005, and 0.001 M and then applied them to films with bromide contents of $x = 0.2$, $x = 0.5$, and x = 0.75. UV/vis was used to track the degradation toward oxygen and light at a selected wavelength (700 nm for $x = 0.2$, 600 nm for $x = 0.5$, and 550 nm for $x = 0.75$), and the data was normalized with respect to the fresh sample of each film and coating combination. The results obtained from this study are presented in Figure 5, which shows a plot of the absorption as a function of aging time for different salt concentrations. Raw absorption data (optical density versus wavelength profiles) are provided in Figure S4. It is clear from the data in Figure 5 that the stability of all samples can be improved by the application of the MAI coating, and the stability enhancement is directly related to the amount of coating used. For example, the tolerance of the perovskite film to oxygen and light progressively increases as the concentration of the MAI salt solution is increased. For the highest concentration applied (0.01 M), all films exhibit enhanced lifetime, where little to no observable degradation occurs over the time frame examined. This implies that using this salt concentration enables the passivation of iodide vacancies in the film.

To investigate whether the increased stability of the films as a result of the salt treatments is due to the passivation of vacancy defects and reduced superoxide generation, the superoxide yield was determined for the samples presented in Figure 6. The results of this study show that for all Br-containing compositions, increasing the salt treatment concentration leads to reduced superoxide yields. Taken together, the data presented in Figures 5 and 6 shows that the perovskites with a higher bromide fraction can be stabilized with a lower concentration of MAI salt treatment. Additionally, as a control, we examined the impact of using methylammonium bromide (MABr) as a stabilizing treatment, which showed no improvement in increasing film stability or in reducing the yield of superoxide.[14] Both $MAPbI_3$ and $MAPbBr_3$ were coated with a 0.0 1 M concentration of MABr, and the results of these experiments are shown in Figure S5.

DOI: 10.1021/acs.chemmater.9b04000
Chem. Mater. 2020, 32, 400−409

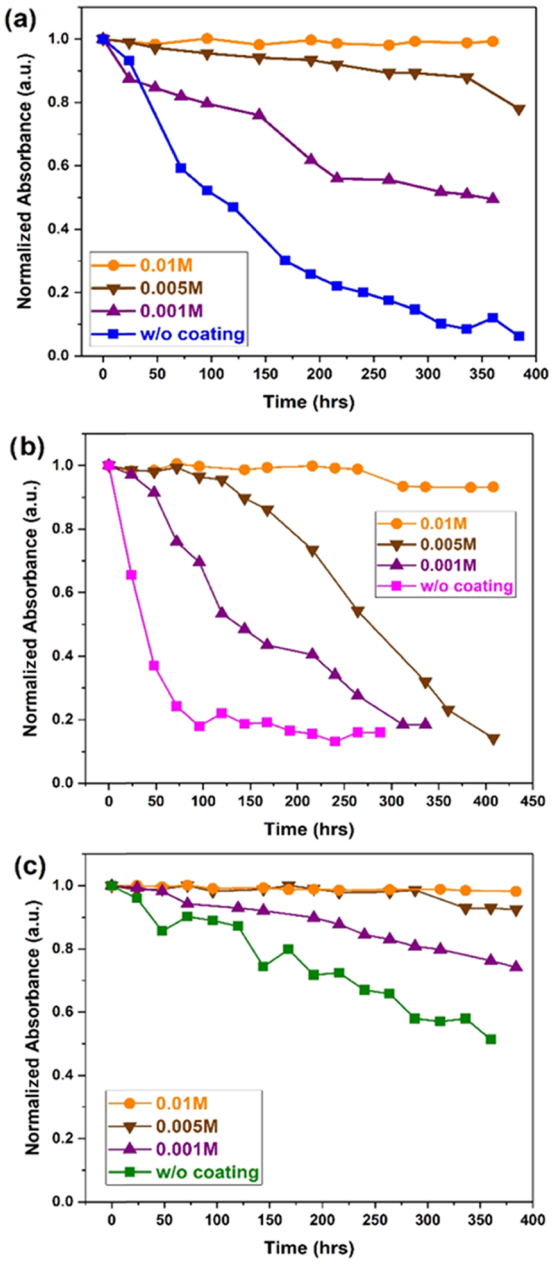

Figure 5. Application of MAI salt coatings (0.01, 0.005, and 0.001 M) to the mixed-halide perovskite system $MAPb(I_{1-x}Br_x)_3$ with compositions of (a) x = 0.2, (b) x = 0.5, and (c) x = 0.75 and the impact on the normalized absorbance decay with exposure to the degradation conditions. As the bromide content increases, the salt concentration required to increase stability decreases.

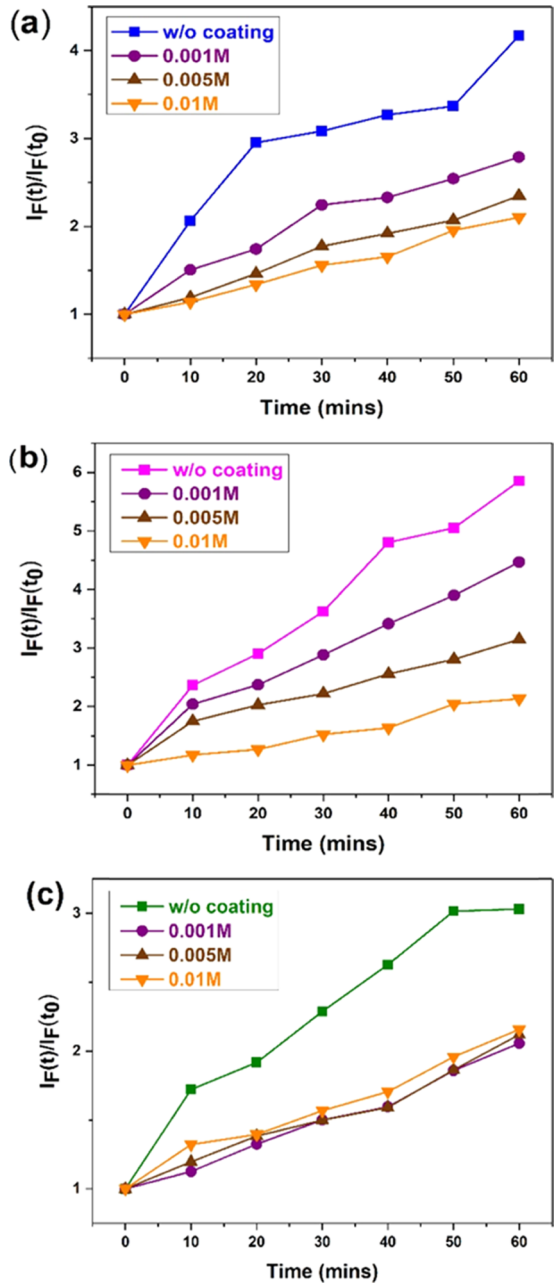

Figure 6. Superoxide generation yields for film compositions of (a) x = 0.2, (b) x = 0.5, and (c) x = 0.75 in $MAPb(I_{1-x}Br_x)_3$ as a function of MAI salt coating (0.01, 0.005, and 0.001 M). Increasing the bromide content reduces the salt concentration required to reduce the yields of superoxide.

To gain further insight into the role of bromide substitution and the impact of film passivation with the MAI salt, time-resolved photoluminescence (TRPL) was employed. Iodide vacancies provide a source for nonradiative recombination, and so when the perovskite film is passivated, the photoluminescence lifetime is expected to increase. Figure S6 shows the TRPL data obtained for a range of four samples with compositions of x = 0, 0.1, 0.2, and 0.5 and with and without an MAI coating of 0.01 M. As can be seen, passivation of the films with the iodide salt leads to an increase in PL lifetime.

Implications for Device Performance. We now consider the effect of bromide substitution on the yield of photoinduced charge separation to the perovskite hole transport material heterojunctions upon exposure to oxygen and light. The rate of charge separation losses has been shown to be directly related to the decay of device performance in operating perovskite solar cells.[34] The yield of hole transfer from the perovskite to the hole-transporting phase, Spiro-OMeTAD, is measured using transient absorption spectroscopy as described in the experimental section. Films with compositions of x = 0, 0.2, 0.5, 0.75, and 1 are examined in an architecture of glass/mp-Al_2O_3/$MAPb(I_{1-x}Br_x)_3$/Spiro-OMeTAD and probed at 1600 nm (tracking concentration of Spiro-OMeTAD hole polarons) following excitation at 458 nm. The change in optical density (ΔOD) value at 1 μs was obtained and then normalized against the starting value, where the sample has not been exposed to the

DOI: 10.1021/acs.chemmater.9b04000
Chem. Mater. 2020, 32, 400−409

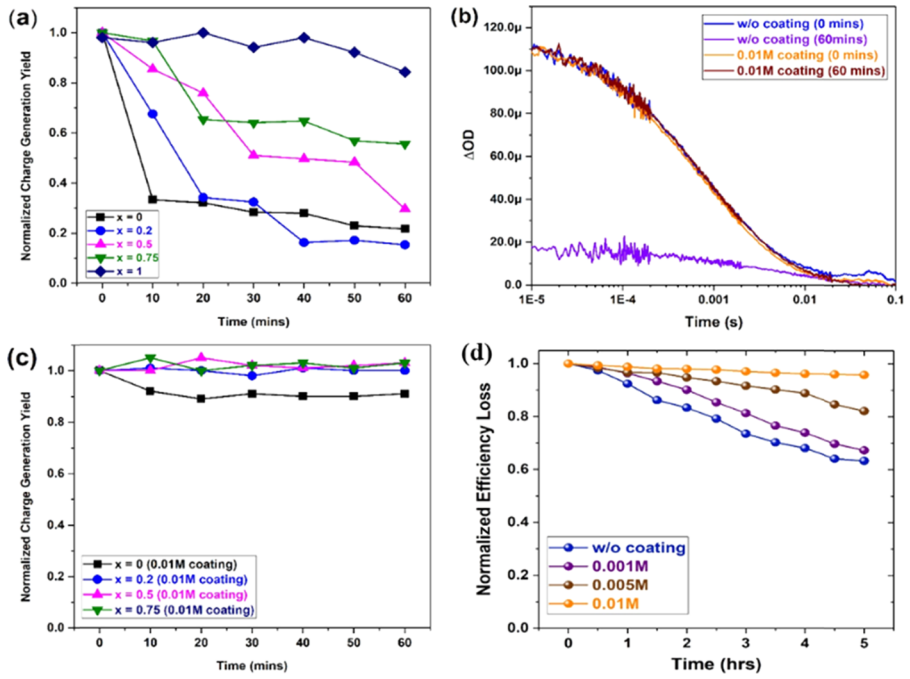

Figure 7. (a) Normalized decay of charge separation yield (ΔOD), obtained from transient absorption spectroscopy for films with compositions $x = 0$, 0.1, 0.2, 0.5, 0.75, and 1. Charge losses are more rapid and significant for compositions with less bromide. (b) Transient absorption spectral traces for $x = 0.2$ film composition, with and without a 0.01 M salt coating fresh (0 min) and after 60 min of exposure to oxygen and illumination. (c) Normalized decay of charge separation losses, obtained from transient absorption spectroscopy for films with compositions $x = 0$, 0.1, 0.2, 0.5, 0.75, and 1 with a 0.01 M MAI salt coating. (d) Normalized device efficiency (normalized power conversion efficiency, PCE) loss for a device employing $x = 0.2$ perovskite composition film.

degradation conditions. The films were exposed to dry air flux and ambient illumination. Measurements were recorded at regular time intervals over the course of an hour and under an inert nitrogen atmosphere.

Figure 7a presents the relationship between normalized charge generation yield ΔOD and time after being exposed to light and oxygen. It is clear that charge separation in the Br-rich films is well maintained even after exposure to light and oxygen. In fact, a close correlation is found between the stability of the film and its Br content. For example, for the fully substituted composition (100% Br), the impact on charge separation yield and therefore degradation is minimal, while in the I-rich perovskites, charge losses are significant within the time frame explored. The time taken for the decay to drop to 50% of its original value is found to be 10, 15, 40, and 60+ min for the films $x = 0$, 0.2, 0.5, and 0.75, respectively. This further demonstrates that Br substitution enhances stability to oxygen and light, allowing films to retain optimum optoelectronic properties for longer periods of time.

We next turn our attention to the effect of iodide salt treatment on the yield of charge separation. To this end, we probed the mixed-halide perovskite films with transient absorption spectroscopy after treating them with a 0.01 M MAI salt solution. Figure 7b shows the ΔOD as a function of time for the 50% Br composition, with and without a salt coating before and after 60 min of exposure to dry air flux and illumination. We note that the decay traces presented in Figure 7b are indicative of the recombination of electrons (or holes) in the perovskite with holes (or electrons) in the transport layers. Moreover, the data in Figure 7b shows that the uncoated film undergoes degradation, where the initial amplitude of the signal (ΔOD) decreases significantly after an hour of exposure to light and oxygen. In contrast, no such drop in the initial amplitude of the signal is seen in the film passivated with the MAI salt solution. Figure 7c presents the relationship between ΔOD (at 1 μs) and aging time for perovskite films of $x = 0$, 0.2, 0.5, and 0.75, with and without a 0.01 M salt coating. Note that all raw TAS traces are provided in Figure S7. It is clear from the data presented in Figure 7c that film passivation via MAI salt solutions generates more stable films that retain their initial charge generation capabilities.

Finally, we consider the effect of film passivation via MAI salts on the stability of mixed-halide perovskite solar cell devices. Devices composed of the 20% bromide composition perovskite were fabricated and treated with MAI salt solutions of 0, 0.001, 0.005, and 0.01 M to generate four devices. The power conversion efficiency (PCE) of these devices was monitored as a function of exposure to oxygen and light, and the normalized PCE as a function of time is plotted in Figure 7d. We note that the current−voltage curves are collected under AM1.5 simulated light and presented in Figure S8 and Table S5. The data presented in Figure 7d confirms that mixed-halide devices can be stabilized by the application of the salt coating. In addition, increasing the concentration of the salt coating progressively increases the stability of the solar cells.

CONCLUSIONS

Our combined experimental−computational study using ab initio simulation and spectroscopy techniques improves our fundamental understanding of the degradation behavior of mixed iodide−bromide perovskite solar cells and indicates design rules for enhancing their long-term stability. Our systematic investigation reveals the following key results:

(a) Absorbance spectroscopy shows that as the Br content in the $MAPb(I_{1-x}Br_x)_3$ system is increased, the material

DOI: 10.1021/acs.chemmater.9b04000
Chem. Mater. 2020, 32, 400−409

stability toward oxygen and light also increases, which correlates with the decreasing yield of superoxide species. Isothermal gravimetric analysis and time-resolved single photon counting show that as the Br content is increased, the amount of oxygen incorporation into perovskite films decreases significantly. This partly accounts for the reduced superoxide yields observed for higher Br substitution levels.

(b) Ab initio simulations on $MAPb(I_{1-x}Br_x)_3$ show that the degradation reaction involving superoxide species leading to water, lead halide, and methylamine formation is energetically favorable and exothermic for pure $MAPbI_3$ but becomes less favorable with increasing Br content. Indeed, for pure $MAPbBr_3$, the degradation reaction is unfavorable and endothermic. This may be related to structural factors: the shorter and stronger N−H...Br hydrogen bonds found between the $CH_3NH_3^+$ cation and Br ions would promote greater structural stability on bromide substitution.

(c) Iodide salt treatment was employed to promote greater stability of perovskites. We find that thin-film passivation with MAI salts leads to enhanced stabilities of mixed-halide perovskite films and solar cell devices.

METHODS

Materials. All chemicals were used as received, including 99% of PbI_2 (Sigma-Aldrich), HI (57% in water, Sigma-Aldrich), $PbBr_2$ (Sigma-Aldrich), MAI (Dyesol), MABr (Dyesol), titanium diisopropoxide bis(acetylacetonate) 97% wt in isopropanol (IPA) (Sigma-Aldrich), spiro-OMeTAD (Lumtec), bis(trifluoromethane)-sulfonimide lithium salt (Li-TFSI, Sigma-Aldrich), 4-*tert*-butylpyridine (TBP), acetone, ethanol, isopropanol, ethanolamine, 2-methoxyethanol, chlorobenzene, γ-butyrolactone (GBL), TiO_2 paste (Dyesol DSL 30 NR-D 30 nm), terpineol, hydroethidine, toluene, dimethyl sulfoxide (DMSO), and acetonitrile.

$MAPbI_3$ and $MAPbBr_3$ Solutions and Film Fabrication. MAI (0.25 g) and 0.78 g of PbI_2 were mixed in a 1:1 mole ratio in 1.4 mL of anhydrous GBL and 0.6 mL of DMSO for 1 h at 60 °C. After that, they were left to precipitate overnight. The solution was filtered out with a 0.2 μm membrane in a small plastic tube. This solution was then pipetted into two consecutive spin steps under a nitrogen atmosphere in a glovebox. The first spin cycle was performed at 2000 rpm, 2000 rpm s^{-1} for 30 s followed by 4000 rpm, 4000 rpm s^{-1} for 30 s. During the second step, the substrate was treated with dry toluene (approximately 500 mL) drop-casting. The film was heated at 100 °C for 10 min. The color of the films changed from yellow to black immediately after being placed on the hot plate. It is noted that it is entirely possible that while transporting and measuring, moisture started to corrode $MAPbI_3$ even though both samples are mostly degraded under a dry air environment. To minimize the amount of moisture getting into the films, the aged films were kept in a closed container with an excess of Si-drying agents underneath, before any characterization techniques were performed. $MAPbBr_3$ solutions and films were created using the exact same method as described above, except using the bromide derivatives, MABr and $PbBr_2$.

$MAPb(I_{1-x}Br_x)_3$ Film Fabrication. Stock solutions of $MAPbI_3$ and $CH_3NH_3PbBr_3$ were prepared by dissolving stoichiometric ratios of PbX_2 and MAX_3 (X = I, Br) in a DMSO and GBL solution (7:3) at 1.25 M concn and stirred for 60 min at 50 °C and room temperature, respectively. To obtain a range of composition in $MAPb(I_{1-x}Br_x)_3$, stock solutions were combined in the desired volumetric ratios. Thin-film samples were prepared on glass using an antisolvent technique adapted from a previously reported method. Glass was washed in soap, acetone, and 2-propanol followed by a 10 min oxygen plasma treatment. The perovskite precursor solution was coated using a spin coating procedure using two speeds where toluene was dripped onto the surface during the second step and then dried at 100 °C post deposition.

Spiro-OMeTAD. The HTM solution was prepared by dissolving 72 mg of spiro-OMeTAD in anhydrous 1 mL of chlorobenzene solution. In the case of device fabrication purposes, 32 μL of Li-TFSI precursor solution (175 mg of Li-TFSI powder in 1 mL of acetonitrile) and 10 μL of 4-*tert*-butylpyridine (TBP) were mixed with the Spiro-OMeTAD. The solution was then filtered with a 0.2 μm membrane in a small plastic tube. It was then spun at 4000 rpm, 4000 rpm s^{-1} for 40 s. For the TAS or UV−vis measurements, the films were measured immediately after the fabrication process.

Film Coatings. Iodide salt solutions were prepared by dissolving the iodide salt (MAI or MABr) in a 1:4 solvent mixture of IPA to chlorobenzene. Of this solution, 100 μL was then dripped onto predeposited perovskite films with a 20 s loading time before spinning at 4000 rpm and annealing at 100 °C for 5 min.

Aging Conditions. Films were sealed in a controlled environment, where dry air was gassed through for the duration of the degradation, and illumination was provided by a tungsten lamp equipped with a UV-blocking filter as previously reported.

Characterizations. UV−vis measurements were carried out using a UV−vis spectrometer (PerkinElmer) in the wavelength range from 400 to 900 nm with a scan speed of 480 nm per minute with 1 nm data intervals and cycle times of 1 s. Its slit width was 1.0 nm. TAS measurements were performed with a 567 nm dye and a GL-301 dye laser (Photon Technology International, TSI) through an oscilloscope (TG330 Function generator with 3 MHz-Generator, 120 MHz counter/sweep). The frequency of the laser pulse was 4 Hz. The pulse was generated with a light source (Bentham IL 1 illuminator) and a voltage of approximately 12.3 V (Bentham 605). The signal size was filtered with a long-pass filter monochromator (Thorlabs) and an optical shielding filter. Each reading was measured at 10 ms time scales for 64 averages for 10 times with a pulse power of 25 μJ cm^{-2}. The aged sample was illuminated against a tungsten halogen lamp (Thorlabs) with an approximate power of 20 mW cm^{-2} with a 400 nm long-pass optical filter throughout the experiments. Each sample was also purged with dry compressed air (< 2 ppm moisture) during the aging conditions.

Superoxide probe testing was achieved by dissolving 10 mL of stock solution (31.7 μM) of the hydroethidine probe in 10 mL of dry toluene. Sonication was used to facilitate miscibility. Perovskite films were submerged into this solution. Photoluminescence spectra were recorded with an excitation wavelength of 520 nm and a slit width of 10 mm on a Horiba Jobin-Yvon Fluorolog-3 spectrofluorometer. The film was illuminated with visible light through a 400 nm long-pass optical filter throughout the experiment. A tungsten halogen lamp provided illumination. The light intensity was approximately 1.5 mW cm^{-2}. Both superoxide yield and UV−vis studies were repeated 3 times to check reproducibility. We note that the same trends were observed in all cases.

TAS measurements were performed with a 567 nm dye and a GL-301 dye laser through an oscilloscope (TG330 Function generator with 3 MHz-Generator, 120 MHz counter/sweep). The frequency of the laser pulse was 4 Hz, and it was generated with a Bentham IL 1 illuminator and a voltage of approximately 12.3 V. The signal size was filtered with a long-pass filter monochromator and an optical shielding filter. Each measurement was measured at 10 ms time scales for 64 averages for 10 times with a pulse power of 25 uJ cm^{-2}. Photoluminescence measurements were performed by placing perovskite samples on a Horiba Jobin-Yvon Fluorolog-3 spectrofluorometer with the same settings as the superoxide probe measurements.

Ab Initio Simulations. To accurately describe the disorder in $MAPb(I_{1-x}Br_x)_3$, a symmetry-adapted ensemble of configurations was used as implemented in the site occupancy disorder program.[69] Geometric optimizations of the generated structures were performed using density functional theory (DFT) with the Vienna ab initio simulation package (VASP).[70,71] Electronic exchange and correlation were modeled with the Perdew−Burke−Ernzerhof (PBE) functional,[72] with van der Waals (vdW) corrections via the Tkatchenko−Sheffler electrodynamic screening method.[73] A high kinetic energy cutoff of 520 eV was used. Geometry optimizations were performed on the 48-atom tetragonal unit cell, and a Γ-centered grid of 4 × 4 × 3 **k**-points was

DOI: 10.1021/acs.chemmater.9b04000
Chem. Mater. 2020, 32, 400−409

employed for Brillouin-zone integrations. The ionic positions were relaxed until the forces were less than 0.01 eV $Å^{-1}$ on each atom. The configuration with the highest probability at 300 K was then investigated further using a 2 × 2 × 1 supercell (giving a tetragonal cell of 192 atoms) in the numeric atom-centered basis set all-electron code FHI-AIMS.[74,75] Tight basis sets were used with tier 2 basis functions for all species using the PBE exchange−correlation functional and Tkatchenko−Sheffler electrodynamic screening scheme consistent with the geometry optimizations performed in VASP. Relativistic effects were considered using an atomic zeroth-order regular approximation.[74] A Γ-centered grid of 2 × 2 × 3 **k**-points was used for sampling, which was tested for convergence. O_2 absorption was modeled at equatorial sites over apical sites as these were shown to be more favorable by 0.2 eV. To determine the spin state of the oxygen atoms, we constrained the difference in the number of up- and down-spin electrons, corresponding to 0 for nonmagnetic, 1 for the low spin state, and 2 μ_B for the high spin state. Initial oxygen incorporation onto a vacancy site leads to a low spin state (1 μ_B), with photoexcitation shown to lead to a nonmagnetic ground state. Structures were relaxed with a convergence criterion of 10^{-4} eV $Å^{-1}$ for forces, 10^{-5} eV $Å^{-1}$ for the electron density, and 10^{-7} eV for the total energy. The virtual-crystal approximation[76] was employed to model photoexcitation in the charged systems; this ensures that the Fermi level does not change in the doped system.[77] Using this method, we model the positively charged iodide vacancies by distributing the charge uniformly over the Pb atoms. The nuclear number of all of the Pb atoms is reduced in the supercell by $\Delta Z_{Pb} = -q/N_{Pb}$, where q is the charge of the iodide vacancy (+1) and N_{Pb} is the number of Pb atoms in the supercell. This leads to the introduction of vacant states at the valence band maximum.

■ ASSOCIATED CONTENT

Supporting Information

The Supporting Information is available free of charge at https://pubs.acs.org/doi/10.1021/acs.chemmater.9b04000.

Results showing the normalized weight increase in $MAPb(I_{1-x}Br_x)_3$ when exposed to air; calculated degradation reaction energies; configurational disorder and the energy of mixing; variation in calculated lattice parameters as a function of the Br content; raw absorbance data, UV−vis absorption spectroscopy, time-resolved photoluminescence, and transient absorption spectroscopy; calculated H-bond distances and current−voltage curves (PDF)

■ AUTHOR INFORMATION

Corresponding Authors

*E-mail: m.s.islam@bath.ac.uk @SaifulChemistry (M.S.I.).
*E-mail: s.a.haque@imperial.ac.uk (S.A.H.).

ORCID

Saif A. Haque: 0000-0001-5483-3321
M. Saiful Islam: 0000-0003-3882-0285

Author Contributions

§A.A. and N.A. contributed equally to this work.

Author Contributions

All authors have given approval to the final version of the manuscript.

Notes

The authors declare no competing financial interest.

■ ACKNOWLEDGMENTS

M.S.I. acknowledges support from the EPSRC for the Energy Materials Programme grant (EP/K016288) and Archer HPC facilities through the Materials Chemistry Consortium (EP/L000202). S.A.H. acknowledges financial support from EPRSC via EP/M023532/1, EP/K010298/1, and EP/K030671/1 grants. M.S.I. and S.A.H. acknowledge the joint EPSRC grant EP/R020485/1. The authors thank D. Ghosh and J. Dawson for their useful discussions.

■ REFERENCES

(1) Kim, H.-S.; Lee, C.-R.; Im, J.-H.; Lee, K.-B.; Moehl, T.; Marchioro, A.; Moon, S.-J.; Humphry-Baker, R.; Yum, J.-H.; Moser, J. E.; Gräetzel, M.; Park, N.-G. Lead Iodide Perovskite Sensitized All-Solid-State Submicron Thin Film Mesoscopic Solar Cell with Efficiency Exceeding 9%. *Sci. Rep.* **2012**, *2*, 591.

(2) Sadhanala, A.; Deschler, F.; Thomas, T. H.; Dutton, S. E.; Goedel, K. C.; Hanusch, F. C.; Lai, M. L.; Steiner, U.; Bein, T.; Docampo, P.; Cahen, D.; Friend, R. H. Preparation of Single-Phase Films of $CH_3NH_3Pb(I_{1-x}Br_x)_3$ with Sharp Optical Band Edges. *J. Phys. Chem. Lett* **2014**, *5*, 2501−2505.

(3) Aharon, S.; El Cohen, B.; Etgar, L. Hybrid Lead Halide Iodide and Lead Halide Bromide in Efficient Hole Conductor Free Perovskite Solar Cell. *J. Phys. Chem. C* **2014**, *118*, 17160−17165.

(4) Etgar, L.; Gao, P.; Qin, P.; Gräetzel, M.; Nazeeruddin, M. K. A hybrid lead iodide perovskite and lead sulfide QD heterojunction solar cell to obtain a panchromatic response. *J. Mater. Chem. A* **2014**, *2*, 11586−11590.

(5) Jeon, N. J.; Noh, J. H.; Yang, W. S.; Kim, Y. C.; Ryu, S.; Seo, J.; Seok, S. I. Compositional engineering of perovskite materials for high-performance solar cells. *Nature* **2015**, *517*, 476−480.

(6) Li, B.; Li, Y.; Zheng, C.; Gao, D.; Huang, W. Advancements in the stability of perovskite solar cells: degradation mechanisms and improvement approaches. *RSC Adv.* **2016**, *6*, 38079−38091.

(7) Zarick, H. F.; Soetan, N.; Erwin, W. R.; Bardhan, R. Mixed halide hybrid perovskites: a paradigm shift in photovoltaics. *J. Mater. Chem. A* **2018**, *6*, 5507−5537.

(8) Ji, L.; Hsu, H.-Y.; Lee, J. C.; Bard, A. J.; Yu, E. T. High-Performance Photodetectors Based on Solution-Processed Epitaxial Grown Hybrid Halide Perovskites. *Nano Lett.* **2018**, *18*, 994−1000.

(9) Kamat, P. V. Hybrid Perovskites for Multifunction Tandem Solar Cells and Solar Fuels. A Virtual Issue. *ACS Energy Lett.* **2018**, *3*, 28−29.

(10) Jodlowski, A. D.; Roldán-Carmona, C.; Grancini, G.; Salado, M.; Ralaiarisoa, M.; Ahmad, S.; Koch, N.; Camacho, L.; de Miguel, G.; Nazeeruddin, M. K. Large guanidinium cation mixed with methylammonium in lead iodide perovskites for 19% efficient solar cells. *Nat. Energy.* **2017**, *2*, 972−979.

(11) Jeon, T.; Kim, S. J.; Yoon, J.; Byun, J.; Hong, H. R.; Lee, T.-W.; Kim, J.-S.; Shin, B.; Kim, S. O. Hybrid Perovskites: Effective Crystal Growth for Optoelectronic Applications. *Adv. Energy Mater.* **2017**, *7*, 1602596.

(12) Huang, J.; Yuan, Y.; Shao, Y.; Yan, Y. Understanding the physical properties of hybrid perovskites for photovoltaic applications. *Nat. Rev. Mater.* **2017**, *2*, 17042.

(13) Xu, F.; Zhang, T.; Li, G.; Zhao, Y. Mixed cation hybrid lead halide perovskites with enhanced performance and stability. *J. Mater. Chem. A* **2017**, *5*, 11450−11461.

(14) Saliba, M.; Matsui, T.; Seo, J.-Y.; Domanski, K.; Correa-Baena, J.-P.; Nazeeruddin, M. K.; Zakeeruddin, S. M.; Tress, W.; Abate, A.; Hagfeldt, A.; Grätzel, M. Cesium-containing triple cation perovskite solar cells: improved stability, reproducibility and high efficiency. *Energy Environ. Sci.* **2016**, *9*, 1989−1997.

(15) Seok, S. I.; Grätzel, M.; Park, N. G. Methodologies toward Highly Efficient Perovskite Solar Cells. *Small* **2018**, *14*, 1704177.

(16) Jena, A. K.; Kulkarni, A.; Miyasaka, T. Halide Perovskite Photovoltaics: Background, Status, and Future Prospects. *Chem. Rev.* **2019**, *119*, 3036−3103.

(17) Kalaiselvi, C. R.; Muthukumarasamy, N.; Velauthapillai, D.; Kang, M.; Senthil, T. S. Importance of halide perovskites for next generation solar cells—A review. *Mater. Lett.* **2018**, *219*, 198−200.

(18) Kim, D. H.; Whitaker, J. B.; Li, Z.; van Hest, M.; Zhu, K. Outlook and Challenges of Perovskite Solar Cells toward Terawatt-Scale Photovoltaic Module Technology. *Joule* **2018**, *2*, 1437−1451.

DOI: 10.1021/acs.chemmater.9b04000
Chem. Mater. 2020, 32, 400−409

(19) Christians, J. A.; Miranda Herrera, P. A.; Kamat, P. V. Transformation of the Excited State and Photovoltaic Efficiency of $CH_3NH_3PbI_3$ Perovskite upon Controlled Exposure to Humidified Air. *J. Am. Chem. Soc.* **2015**, *137*, 1530−1538.
(20) Christians, J. A.; Manser, J. S.; Kamat, P. V. Best Practices in Perovskite Solar Cell Efficiency Measurements. Avoiding the Error of Making Bad Cells Look Good. *J. Phys. Chem. Lett.* **2015**, *6*, 852−857.
(21) Zhang, T.; Meng, X. Y.; Bai, Y.; Xiao, S.; Hu, C.; Yang, Y. L.; Chen, H. N.; Yang, S. H. Profiling the organic cation-dependent degradation of organolead halide perovskite solar cells. *J. Mater. Chem. A* **2017**, *5*, 1103−1111.
(22) Yuan, H.; Debroye, E.; Janssen, K.; Naiki, H.; Steuwe, C.; Lu, G.; Moris, M.; Orgiu, E.; Uji-i, H.; De Schryver, F.; Samorì, P.; Hofkens, J.; Roeffaers, M. Degradation of Methylammonium Lead Iodide Perovskite Structures through Light and Electron Beam Driven Ion Migration. *J. Phys. Chem. Lett.* **2016**, *7*, 561−566.
(23) Kim, N. K.; Min, Y. H.; Noh, S.; Cho, E.; Jeong, G.; Joo, M.; Ahn, S. W.; Lee, J. S.; Kim, S.; Ihm, K.; Ahn, H.; Kang, Y.; Lee, H. S.; Kim, D. Investigation of Thermally Induced Degradation in $CH_{3N}H3_PbI_3$ Perovskite Solar Cells using in-situ Synchrotron Radiation Analysis. *Sci. Rep.* **2017**, *7*, 4645.
(24) Domanski, K.; Alharbi, E. A.; Hagfeldt, A.; Grätzel, M.; Tress, W. Systematic investigation of the impact of operation conditions on the degradation behaviour of perovskite solar cells. *Nat. Energy* **2018**, *3*, 61−67.
(25) Farooq, A.; Hossain, I. M.; Moghadamzadeh, S.; Schwenzer, J. A.; Abzieher, T.; Richards, B. S.; Klampaftis, E.; Paetzold, U. W. Spectral Dependence of Degradation under Ultraviolet Light in Perovskite Solar Cells. *ACS Appl. Mater. Interfaces* **2018**, *10*, 21985−21990.
(26) Kye, Y. H.; Yu, C. J.; Jong, U. G.; Chen, Y.; Walsh, A. Critical Role of Water in Defect Aggregation and Chemical Degradation of Perovskite Solar Cells. *J. Phys. Chem. Lett.* **2018**, *9*, 2196−2201.
(27) Marronnier, A.; Lee, H.; Kim, M.; Eypert, C.; Gaston, J. P.; Roma, G.; Tondelier, D.; Geffroy, B.; Bonnassieux, Y. Electrical and optical degradation study of methylammonium-based perovskite materials under ambient conditions. *Sol. Energy Mater. Sol. Cells* **2018**, *178*, 179−185.
(28) Xiang, Y. R.; Zhang, F.; He, J. J.; Lian, J. R.; Zeng, P. J.; Song, J.; Qu, J. L. Light-current-induced acceleration of degradation of methylammonium lead iodide perovskite solar cells. *J. Power Sources* **2018**, *384*, 303−311.
(29) Alberti, A.; Deretzis, I.; Mannino, G.; Smecca, E.; Sanzaro, S.; Numata, Y.; Miyasaka, T.; La Magna, A. Revealing a Discontinuity in the Degradation Behavior of $CH_3NH_3PbI_3$ during Thermal Operation. *J. Phys. Chem. C* **2017**, *121*, 13577−13585.
(30) Nickel, N. H.; Lang, F.; Brus, V. V.; Shargaieva, O.; Rappich, J. Unraveling the Light-Induced Degradation Mechanisms of $CH_{3N}H_{3P}bI_3$ Perovskite Films. *Adv. Electron. Mater.* **2017**, *3*, 1700158.
(31) Yang, J. M.; Luo, Y. X.; Bao, Q. Y.; Li, Y. Q.; Tang, J. X. Recent Advances in Energetics and Stability of Metal Halide Perovskites for Optoelectronic Applications. *Adv. Mater. Interfaces* **2019**, *6*, 1801351.
(32) Aristidou, N.; Eames, C.; Sanchez-Molina, I.; Bu, X. N.; Kosco, J.; Islam, M. S.; Haque, S. A. Fast oxygen diffusion and iodide defects mediate oxygen-induced degradation of perovskite solar cells. *Nat. Commun.* **2017**, *8*, 15218.
(33) Aristidou, N.; Sanchez-Molina, I.; Chotchuangchutchaval, T.; Brown, M.; Martinez, L.; Rath, T.; Haque, S. A. The Role of Oxygen in the Degradation of Methylammonium Lead Trihalide Perovskite Photoactive Layers. *Angew. Chem., Int. Ed.* **2015**, *54*, 8208−8212.
(34) Bryant, D.; Aristidou, N.; Pont, S.; Sanchez-Molina, I.; Chotchunangatchaval, T.; Wheeler, S.; Durrant, J. R.; Haque, S. A. Light and oxygen induced degradation limits the operational stability of methylammonium lead triiodide perovskite solar cells. *Energy Environ. Sci.* **2016**, *9*, 1655−1660.
(35) Pont, S.; Bryant, D.; Lin, C. T.; Aristidou, N.; Wheeler, S.; Ma, X. R.; Godin, R.; Haque, S. A.; Durrant, J. R. Tuning $CH_3NH_3Pb(I_{1-x}Br_x)_3$ perovskite oxygen stability in thin films and solar cells. *J. Mater. Chem. A* **2017**, *5*, 9553−9560.
(36) Kulkarni, S. A.; Baikie, T.; Boix, P. P.; Yantara, N.; Mathews, N.; Mhaisalkar, S. Band-gap tuning of lead halide perovskites using a sequential deposition process. *J. Mater. Chem. A* **2014**, *2*, 9221−9225.
(37) Fedeli, P.; Gazza, F.; Calestani, D.; Ferro, P.; Besagni, T.; Zappettini, A.; Calestani, G.; Marchi, E.; Ceroni, P.; Mosca, R. Influence of the Synthetic Procedures on the Structural and Optical Properties of Mixed-Halide (Br, I) Perovskite Films. *J. Phys. Chem. C* **2015**, *119*, 21304−21313.
(38) Gil-Escrig, L.; Miquel-Sempere, A.; Sessolo, M.; Bolink, H. J. Mixed Iodide-Bromide Methylammonium Lead Perovskite-based Diodes for Light Emission and Photovoltaics. *J. Phys. Chem. Lett.* **2015**, *6*, 3743−3748.
(39) Ledinský, M.; Loeper, P.; Niesen, B.; Holovský, J.; Moon, S.-J.; Yum, J.-H.; De Wolf, S.; Fejfar, A.; Ballif, C. Raman Spectroscopy of Organic-Inorganic Halide Perovskites. *J. Phys. Chem. Lett.* **2015**, *6*, 401−406.
(40) Brivio, F.; Caetano, C.; Walsh, A. Thermodynamic Origin of Photoinstability in the $CH_3NH_3Pb(I_{1-x}Br_x)_3$ Hybrid Halide Perovskite Alloy. *J. Phys. Chem. Lett.* **2016**, *7*, 1083−1087.
(41) Yin, T. T.; Fang, Y. N.; Fan, X. F.; Zhang, B. M.; Kuo, J. L.; White, T. J.; Chow, G. M.; Yan, J. X.; Shen, Z. X. Hydrogen-Bonding Evolution during the Polymorphic Transformations in $CH_3NH_3PbBr_3$: Experiment and Theory. *Chem. Mater.* **2017**, *29*, 5974−5981.
(42) Mokhtar, M. Z.; Chen, Q.; Lian, Q.; Lewis, D. J.; Saunders, B. R.; Walton, A. S.; Ke, C. R.; Whittaker, E.; Hamilton, B.; Haque, S. Decoupling Structure and Composition of $CH_3NH_3PbI_{3-x}Br_x$ Films Prepared by Combined One-Step and Two-Step Deposition. *ACS Appl. Energy Mater.* **2018**, *1*, 5567−5578.
(43) Noh, J. H.; Im, S. H.; Heo, J. H.; Mandal, T. N.; Seok, S. I. Chemical Management for Colorful, Efficient, and Stable Inorganic-Organic Hybrid Nanostructured Solar Cells. *Nano Lett.* **2013**, *13*, 1764−1769.
(44) Ansari, F.; Salavati-Niasari, M.; Nazari, P.; Mir, N.; Ahmadi, V.; Nejand, B. A. Long-Term Durability of Bromide-Incorporated Perovskite Solar Cells via a Modified Vapor-Assisted Solution Process. *ACS Appl. Energy Mater.* **2018**, *1*, 6018−6026.
(45) Svanström, S.; Jacobsson, T. J.; Sloboda, T.; Giangrisostomi, E.; Ovsyannikov, R.; Rensmo, H.; Cappel, U. B. Effect of halide ratio and Cs + addition on the photochemical stability of lead halide perovskites. *J. Mater. Chem. A* **2018**, *6*, 22134−22144.
(46) Balakrishna, R. G.; Kobosko, S. M.; Kamat, P. V. Mixed Halide Perovskite Solar Cells. Consequence of Iodide Treatment on Phase Segregation Recovery. *ACS Energy Lett.* **2018**, *3*, 2267−2272.
(47) Gonzalez-Rodriguez, R.; Arad-Vosk, N.; Sa'ar, A.; Coffer, J. L. Phase Control in Mixed Halide Methylammonium Lead Perovskites Using Silicon Nanotube Templates. *J. Phys. Chem. C* **2018**, *122*, 20040−20045.
(48) Pistor, P.; Burwig, T.; Brzusk, C.; Weber, B.; Franzel, W. Thermal stability and miscibility of co-evaporated methyl ammonium lead halide ($MAPbX_3$, X = I, Br, Cl) thin films analysed by in situ X-ray diffraction. *J. Mater. Chem. A* **2018**, *6*, 11496−11506.
(49) Ouafi, M.; Jaber, B.; Atourki, L.; Bekkari, R.; Laanab, L. Improving UV stability of $MAPbI_3$ perovskite thin films by bromide incorporation. *J. Alloys Compd.* **2018**, *746*, 391−398.
(50) Longo, G.; Momblona, C.; La-Placa, M. G.; Gil-Escrig, L.; Sessolo, M.; Bolink, H. J. Fully Vacuum-Processed Wide Band Gap Mixed-Halide Perovskite Solar Cells. *ACS Energy Lett.* **2018**, *3*, 214−219.
(51) Knight, A. J.; Wright, A. D.; Patel, J. B.; McMeekin, D. P.; Snaith, H. J.; Johnston, M. B.; Herz, L. M. Electronic Traps and Phase Segregation in Lead Mixed-Halide Perovskite. *ACS Energy Lett.* **2019**, *4*, 75−84.
(52) Hoke, E. T.; Slotcavage, D. J.; Dohner, E. R.; Bowring, A. R.; Karunadasa, H. I.; McGehee, M. D. Reversible photo-induced trap formation in mixed-halide hybrid perovskites for photovoltaics. *Chem. Sci.* **2015**, *6*, 613−617.
(53) Braly, I. L.; Stoddard, R. J.; Rajagopal, A.; Uhl, A. R.; Katahara, J. K.; Jen, A. K. Y.; Hillhouse, H. W. Current-Induced Phase Segregation

DOI: 10.1021/acs.chemmater.9b04000
Chem. Mater. 2020, 32, 400−409

in Mixed Halide Hybrid Perovskites and its Impact on Two-Terminal Tandem Solar Cell Design. *ACS Energy Lett.* **2017**, *2*, 1841−1847.
(54) Duong, T.; Mulmudi, H. K.; Wu, Y. L.; Fu, X.; Shen, H. P.; Peng, J.; Wu, N. D.; Nguyen, H. T.; Macdonald, D.; Lockrey, M.; White, T. P.; Weber, K.; Catchpole, K. Light and Electrically Induced Phase Segregation and Its Impact on the Stability of Quadruple Cation High Bandgap Perovskite Solar Cells. *ACS Appl. Mater. Interfaces* **2017**, *9*, 26859−26866.
(55) Rehman, W.; McMeekin, D. P.; Patel, J. B.; Milot, R. L.; Johnston, M. B.; Snaith, H. J.; Herz, L. M. Photovoltaic mixed-cation lead mixed-halide perovskites: links between crystallinity, photostability and electronic properties. *Energy Environ. Sci.* **2017**, *10*, 361−369.
(56) Hu, M.; Bi, C.; Yuan, Y.; Bai, Y.; Huang, J. Stabilized Wide Bandgap $MAPbBr_{(x)}I_{(3-x)}$ Perovskite by Enhanced Grain Size and Improved Crystallinity. *Adv. Sci.* **2016**, *3*, 1500301.
(57) Zhou, Y.; Jia, Y. H.; Fang, H. H.; Loi, M. A.; Xie, F. Y.; Gong, L.; Qin, M. C.; Lu, X. H.; Wong, C. P.; Zhao, N. Composition-Tuned Wide Bandgap Perovskites: From Grain Engineering to Stability and Performance Improvement. *Adv. Funct. Mater.* **2018**, *28*, 1803130.
(58) O'Mahony, F. T. F.; Lee, Y. H.; Jellett, C.; Dmitrov, S.; Bryant, D. T. J.; Durrant, J. R.; O'Regan, B. C.; Gräetzel, M.; Nazeeruddin, M. K.; Haque, S. A. Improved environmental stability of organic lead trihalide perovskite-based photoactive-layers in the presence of mesoporous TiO_2. *J. Mater. Chem. A* **2015**, *3*, 7219−7223.
(59) Roldán-Carmona, C.; Gratia, P.; Zimmermann, I.; Grancini, G.; Gao, P.; Gräetzel, M.; Nazeeruddin, M. K. High efficiency methylammonium lead triiodide perovskite solar cells: the relevance of non-stoichiometric precursors. *Energy Environ. Sci.* **2015**, *8*, 3550−3556.
(60) Meggiolaro, D.; Mosconi, E.; De Angelis, F. Mechanism of Reversible Trap Passivation by Molecular Oxygen in Lead-Halide Perovskites. *ACS Energy Lett.* **2017**, *2*, 2794−2798.
(61) Tian, Y.; Peter, M.; Unger, E.; Abdellah, M.; Zheng, K.; Pullerits, T.; Yartsev, A.; Sundstrom, V.; Scheblykin, I. G. Mechanistic insights into perovskite photoluminescence enhancement: light curing with oxygen can boost yield 1000-fold. *Phys. Chem. Chem. Phys.* **2015**, *17*, 24978−24987.
(62) Eames, C.; Frost, J. M.; Barnes, P. R. F.; O'Regan, B. C.; Walsh, A.; Islam, M. S. Ionic transport in hybrid lead iodide perovskite solar cells. *Nat. Commun.* **2015**, *6*, 7497.
(63) Ghosh, D.; Smith, A. R.; Walker, A. B.; Islam, M. S. Mixed A-Cation Perovskites for Solar Cells: Atomic-Scale Insights Into Structural Distortion, Hydrogen Bonding, and Electronic Properties. *Chem. Mater.* **2018**, *30*, 5194−5204.
(64) Brenes, R.; Eames, C.; Bulovic, V.; Islam, M. S.; Stranks, S. D. The Impact of Atmosphere on the Local Luminescence Properties of Metal Halide Perovskite Grains. *Adv. Mater.* **2018**, *30*, 1706208.
(65) Atourki, L.; Vega, E.; Mari, B.; Mollar, M.; Ahsaine, H. A.; Bouabid, K.; Ihlal, A. Role of the chemical substitution on the structural and luminescence properties of the mixed halide perovskite thin $MAPbI_{(3-x)}Br_{(x)}$ $(0 < = x < = 1)$ films. *Appl. Surf. Sci.* **2016**, *371*, 112−117.
(66) Poglitsch, A.; Weber, D. Dynamic disorder in methylammoniumtrihalogenplumbates(II) observed by millimeter-wave spectroscopy. *J. Chem. Phys.* **1987**, *87*, 6373−6378.
(67) Szafrański, M.; Katrusiak, A. Mechanism of Pressure-Induced Phase Transitions, Amorphization, and Absorption-Edge Shift in Photovoltaic Methylammonium Lead Iodide. *J. Phys. Chem. Lett.* **2016**, *7*, 3458−3466.
(68) Jaffe, A.; Lin, Y.; Beavers, C. M.; Voss, J.; Mao, W. L.; Karunadasa, H. I. High-Pressure Single-Crystal Structures of 3D Lead-Halide Hybrid Perovskites and Pressure Effects on their Electronic and Optical Properties. *ACS Cent. Sci.* **2016**, *2*, 201−209.
(69) Grau-Crespo, R.; Hamad, S.; Catlow, C. R. A.; de Leeuw, N. H. Symmetry-adapted configurational modelling of fractional site occupancy in solids. *J. Phys.: Condens. Matter* **2007**, *19*, 256201.
(70) Kresse, G.; Furthmüller, J. Efficient iterative schemes for ab initio total-energy calculations using a plane-wave basis set. *Phys. Rev. B* **1996**, *54*, 11169−11186.
(71) Kresse, G.; Furthmüller, J. Efficiency of ab-initio total energy calculations for metals and semiconductors using a plane-wave basis set. *Comput. Mater. Sci.* **1996**, *6*, 15−50.
(72) Perdew, J. P.; Burke, K.; Ernzerhof, M. Generalized gradient approximation made simple. *Phys. Rev. Lett.* **1996**, *77*, 3865−3868.
(73) Tkatchenko, A.; Ambrosetti, A.; DiStasio, R. A. Interatomic methods for the dispersion energy derived from the adiabatic connection fluctuation-dissipation theorem. *J. Chem. Phys.* **2013**, *138*, 074106.
(74) Blum, V.; Gehrke, R.; Hanke, F.; Havu, P.; Havu, V.; Ren, X. G.; Reuter, K.; Scheffler, M. Ab initio molecular simulations with numeric atom-centered orbitals. *Comput. Phys. Commun.* **2009**, *180*, 2175−2196.
(75) Ren, X. G.; Rinke, P.; Blum, V.; Wieferink, J.; Tkatchenko, A.; Sanfilippo, A.; Reuter, K.; Scheffler, M. Resolution-of-identity approach to Hartree-Fock, hybrid density functionals, RPA, MP2 and GW with numeric atom-centered orbital basis functions. *New J. Phys.* **2012**, *14*, 053020.
(76) Scheffler, M. Lattice relaxations at substitutional impurities in semiconductors. *Physica B+C* **1987**, *146*, 176−186.
(77) Richter, N. A.; Sicolo, S.; Levchenko, S. V.; Sauer, J.; Scheffler, M. Concentration of Vacancies at Metal-Oxide Surfaces: Case Study of MgO(100). *Phys. Rev. Lett.* **2013**, *111*, 045502.

DOI: 10.1021/acs.chemmater.9b04000
Chem. Mater. 2020, 32, 400−409